

In Situ Observation of Acicular Ferrite Nucleation and Growth at Different Cooling Rate in Ti-Zr Deoxidized Steel



YONGKUN YANG, DONGPING ZHAN, HONG LEI, GUOXING QIU, YULU LI, ZHOUHUA JIANG, and HUI SHU ZHANG

The effects of cooling rate on acicular ferrite (AF) nucleation, growth, and inclusion characteristics in Ti-Zr deoxidation steel were studied by utilizing the high temperature confocal laser scanning microscope (HT-CLSM). The results indicated that with the increase of cooling rate, the ferrite start nucleation temperature decreased, and the difference of first nucleation temperature between AF and ferrite side plate (FSP) reduced. When the cooling rate increased to 10.0 °C/s, AF and FSP simultaneously nucleated at 564.5 °C. In addition, the AF actual growth rate rose with the increase of cooling rate and reached 30.13 $\mu\text{m/s}$ at 10.0 °C/s cooling rate. The AF ratio in microstructure increased first and then decreased with the cooling rate increase and was up to the maximum 45.83 pct at 1.0 °C/s cooling rate. For inclusion characteristics, cooling rates had no obvious effect on inclusion types, but had a great influence on inclusions size distribution. With the cooling rate increase, the inclusion average diameter reduced, and diminished to 1.39 μm at 10.0 °C/s cooling rate. Finally, the AF nucleation on the Ti-Zr-Mn-O-S + TiN inclusion could be explained by the low lattice misfit between ferrite and TiN that precipitated on the Ti-Zr-Mn-O-S inclusion surface.

<https://doi.org/10.1007/s11663-019-01668-z>

© The Minerals, Metals & Materials Society and ASM International 2019

I. INTRODUCTION

ACICULAR ferrite (AF) had the chaotic arrangement^[1] and played an important role in refining grain size and improving steel properties.^[2] It was the most desirable microstructural feature in heat affected-zone (HAZ)^[3] and high strength low alloy steel (HSLA).^[4] Previous studies had shown AF nucleation and growth were not only related to inclusions characteristics,^[5,6] but also related to austenite grain size^[7] and cooling rate.^[8] With regard to inclusion characteristics, researchers had found a large number of inclusion types could induce AF nucleation through thermal cycling simulation experiment,^[3,9] deoxidization solidification experiment^[10–12] and welding experiment,^[13,14] ranging

from single inclusions (as TiN,^[15–17] Ti₂O₃,^[18–20] CuS,^[21] *etc.*) to complex non-metallic inclusions (as Zr-Ti oxides,^[3] Mg-Ti-O-MnS,^[12] Al₂O₃-MgO-ZrO₂,^[22] MgO-Al₂O₃-MnS,^[23] *etc.*). The currently recognized mechanisms of inclusion-induced AF nucleation were: (1) inclusion as effective interface reduced the interface energy of ferrite nucleation;^[24] (2) Depletion of austenite stable elements (such as Mn,^[15] C,^[25] *etc.*) or enrichment of ferrite stable elements (such as P,^[10] Si,^[26] *etc.*) near inclusions increased the driving force of ferrite nucleation; (3) thermal strain at inclusions increased the driving force of ferrite nucleation;^[27] and (4) low lattice misfit between inclusion and ferrite reduced the nucleation barrier.^[28] However, with the development of exploratory research, researchers had found that a single theory could not fully explain the phenomenon of inclusion-induced AF nucleation, often two or more theories worked together.^[10,14,23,26]

Cooling rate, as one of factors to control the final microstructure, was significant for AF nucleation and growth.^[29,30] At present, the research on the influence of cooling rate on the phase transition focused on the thermal dilatometry experiment.^[29–32] Although the ferrite nucleation temperature could be determined by the thermal expansion curve,^[33] the nucleation positions and ferrite types could not be accurately judged. Moreover, since the AF growth time and length were

YONGKUN YANG, DONGPING ZHAN, HONG LEI, and ZHOUHUA JIANG are with the School of Metallurgy, Northeastern University, NO. 3-11, Wenhua Road, Heping District, Shenyang, 110819, P.R. China. Contact email: zhandp1906@163.com
GUOXING QIU and YULU LI are with the School of Materials Science and Engineering, Northeastern University, Shenyang 110819, P.R. China. HUI SHU ZHANG is with Metallurgical Engineering College, Liaoning Institute of Science and Technology, Benxi 117004, P.R. China.

Manuscript submitted March 24, 2019.

Article published online September 4, 2019.

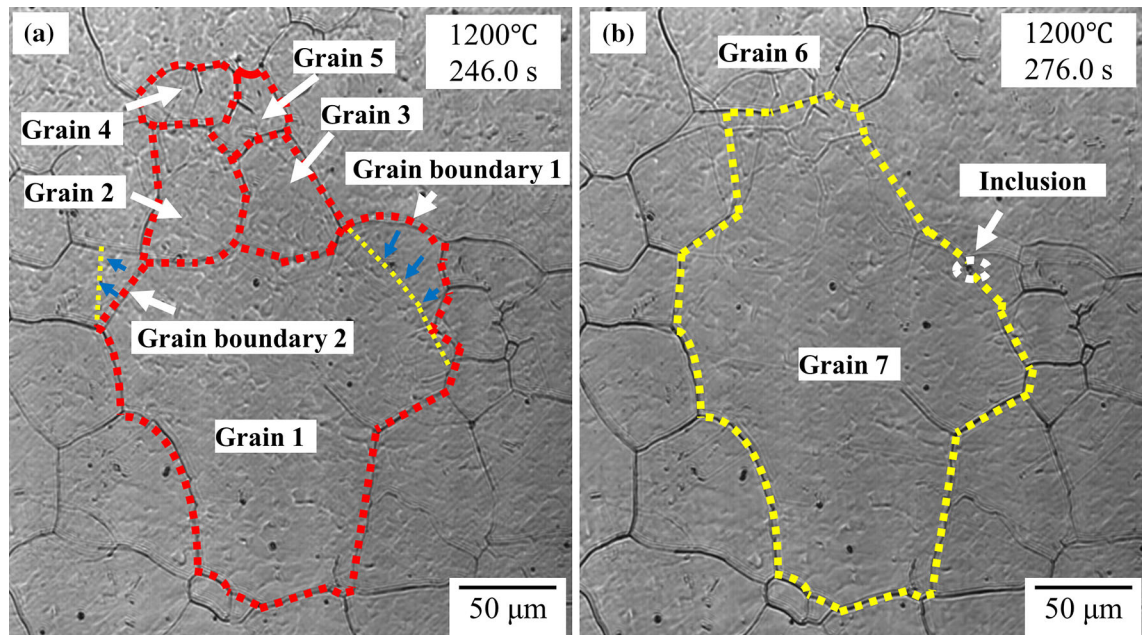


Fig. 1—*In situ* observation of the coalescence of austenite grains at 1200 °C isothermal holding (a) 30 s and (b) 60 s.

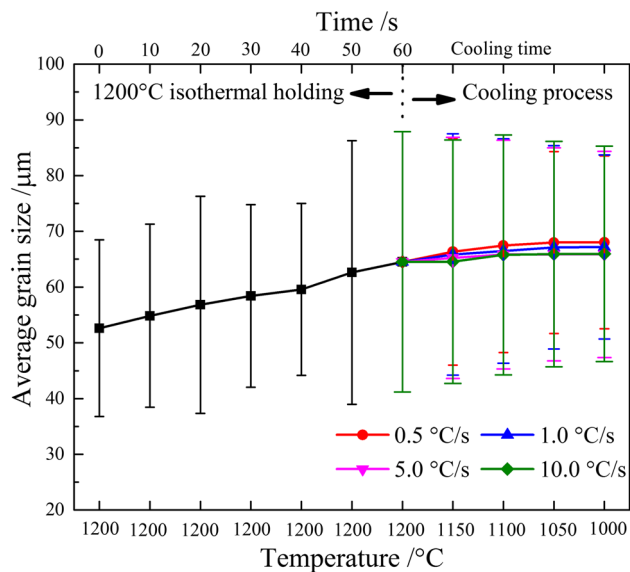


Fig. 2—Relationship between austenite grain sizes with the isothermal holding time and cooling time.

unable exactly matched, the AF growth rate also cannot be obtained. Based on the these mentioned inability to observe ferrite nucleation and growth, high temperature confocal laser scanning microscope (HT-CLSM) technique was considered as a powerful tool to observe phase transformations and microstructural evolution in real time during heating, isothermal holding, and cooling process.^[34,35] For the first time, Hanamura *et al.*^[36] used this method to observe the nucleation of intragranular ferrite on inclusions, and confirmed the thermodynamic calculation results by observation.

Subsequently, this method was increasingly popular in studying AF formation due to its visibility of phase transitions on the sample surface. Zhang *et al.*^[37] observed the evolution of AF by *in situ* in Ti-containing C-Mn steel, and systematically analyzed the influence of austenite grain size, alloy content and inclusions on the nucleation and growth of AF. On this basis, he and his co-workers also analyzed the effect of different cooling rates on AF transformation temperature of low carbon boron-treated steel by the same way. They believed the optimal cooling rate depended on the austenite grain size and the B content in the steel.^[8] Mu *et al.*^[38] combined *in situ* observation with differential scanning calorimetry (DSC) to observe the nucleation and growth of intragranular ferrite during austenite decomposition. The effects of inclusion types and cooling rate on the initial ferrite transformation and final structure were discussed. It was confirmed the application of DSC could supplement more phase transformation information for *in situ* observation. Zou *et al.*^[39] observed the growth of ferrite lath *in situ*. Combining with image processing, the growth rate of ferrite at different cooling rates was obtained in HAZ of shipbuilding steel containing Mg.

The previous studies have confirmed that for different deoxidized alloyed steel, the effects of inclusion characteristics and cooling rate on AF nucleation and growth were different. Ti-Zr oxides, as the products of Ti-Zr complex deoxidation, were small in size and uniformly distributed, which could be used as AF nucleation cores.^[3,40] Therefore, the purpose of this paper was to choose Ti-Zr deoxidation steel as the research object, systematically investigating the effects of cooling rate and inclusion characteristics on the AF nucleation and growth, analyzing the relationship between cooling rate

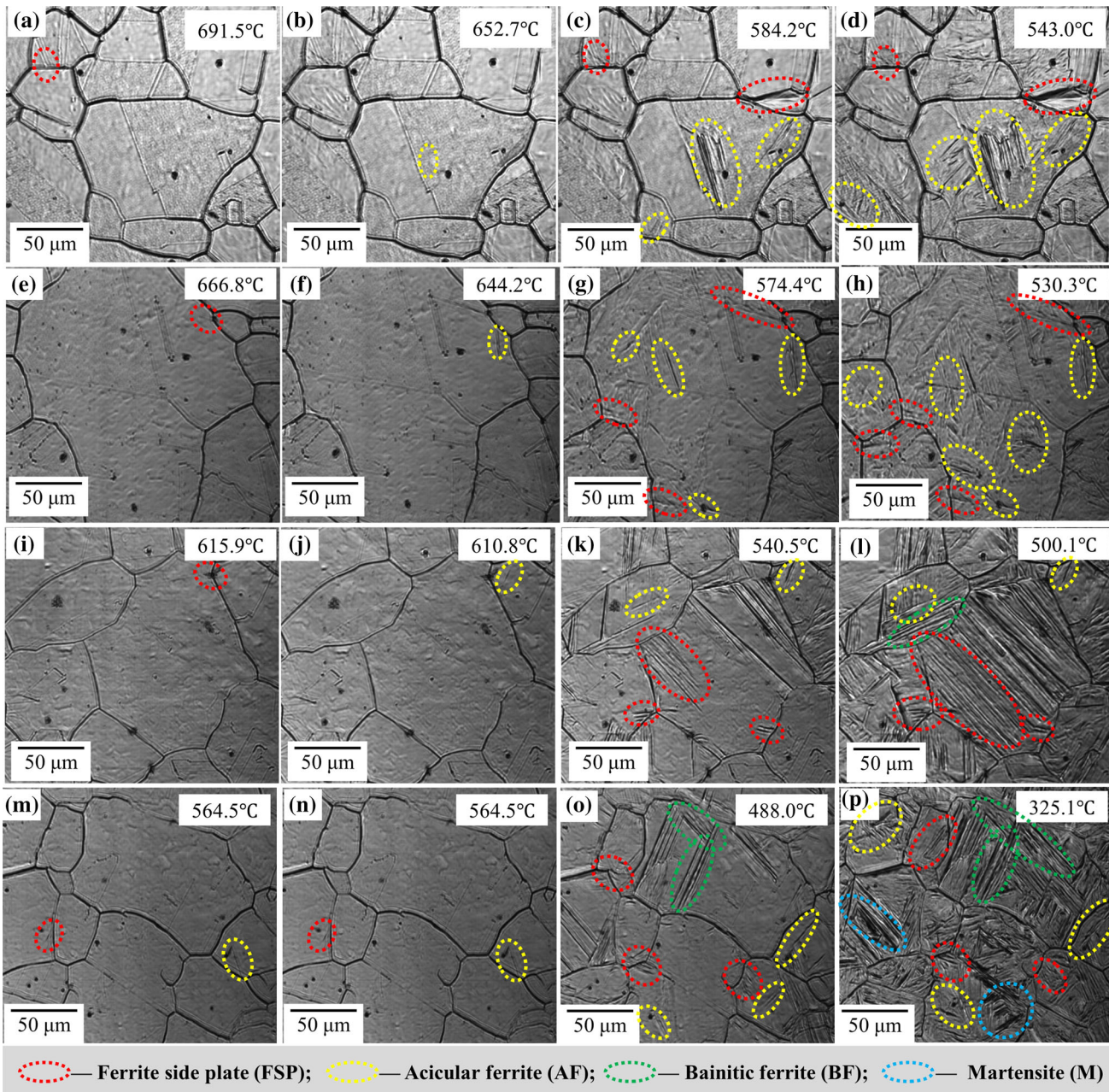


Fig. 3—Typical HT-CLSM images of FSP, AF nucleation and growth at different cooling rate (a) through (d) 0.5 °C/s, (e) through (h) 1.0 °C/s, (i) through (l) 5.0 °C/s and (m) through (p) 10.0 °C/s.

and AF first transition temperature and growth rate, exploring the inclusion characteristics after re-heating and the mechanism of AF nucleation.

II. EXPERIMENTAL

The experimental steel studied was Ti-Zr deoxidized steel, which was prepared by melting in a 30 kg vacuum induction furnace. The chemical compositions of the experimental steel were Fe-0.21C-0.28Si-0.80Mn-0.50Cr-0.57Ni-0.17Mo-0.005S-0.033Ti-0.002Zr-0.0019O-0.0025N (in mass, pct).

The cylindrical samples, which size of 5 mm in diameter and 3 mm in thickness, were sectioned from the center of the prepared ingot. Before experiment, the surfaces of samples were treated by standard grinding and polishing, and then set into alumina crucibles. The *in situ* observation experiments were carried out by using HT-CLSM (VL2000DX-SVF17SP/15FTC) with pure Ar (purity > 99.9999 pct) as furnace atmosphere. The temperature of the studied sample was measured by an R-type thermocouple positioned at bottom of the crucible. It should be pointed out that there was a temperature difference between the bottom and the surface of sample, which was around 20 °C, due to the

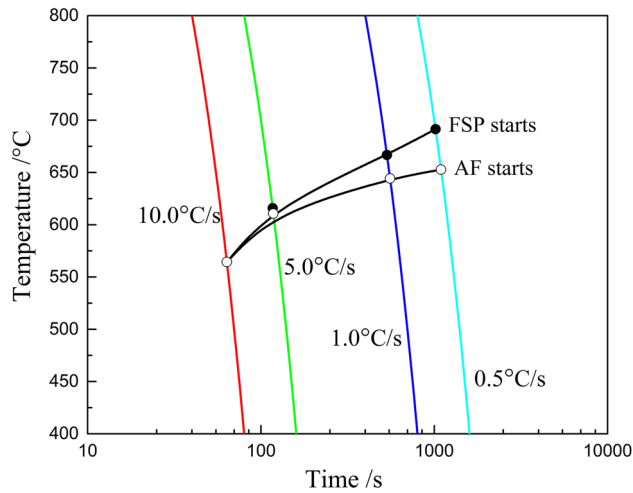


Fig. 4—Schematic CCT diagram for Ti-Zr deoxidation steel.

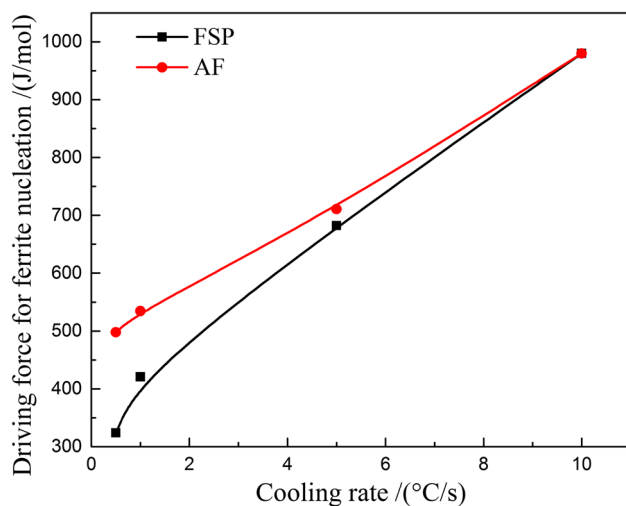


Fig. 5—Relationship between driving force for ferrite nucleation and cooling rate.

thickness of sample.^[34,38] The target heating temperature was chosen as 1200 °C that was the commonly used heating temperature for most HSLA steels to obtain satisfactory microstructure before hot deformation. The samples were heated to target temperature at rate of 10.0 °C/s, and isothermal held for 60 seconds, then immediately continuous cooling to 300 °C with cooling rate of 0.5, 1.0, 5.0, and 10.0 °C/s. In order to observe austenite grain growth, decomposition and the detailed information of ferrite nucleation and growth, the images of samples were recorded at 2 frames per second.

The austenite grain size during isothermal holding and continuous cooling process was measured by image process software, Image Pro Plus 6.0 (IPP 6.0). After heating cycle, the samples were treated by standard grinding and polishing, and the inclusion characteristics of samples were analyzed by using scanning electron microscope (SEM, ULTRA PLUS) equipped with an

energy-dispersive spectrometer (EDS). Then the samples were etched by 4 pct Nital (volume fraction) to observe and confirm the microstructure by SEM-EDS, optical microscope (OM, OLYMPUS DSX500) and micro-hardness tester (FUTURE-TECH FM-700). The proportions of various types of microstructure were determined by systematic manual point count basing on the ASTM-E562-02 standard test method. To reduce the errors, at least 10 images for each sample were chosen.

III. RESULTS AND DISCUSSION

A. Austenite Grains Growth Behavior

Figure 1 showed the *in situ* observation of austenite grains growth during isothermal holding at 1200 °C, in which Figures 1(a) and (b) were holding time for 30 and 60 seconds, respectively. From the Figure 1, the austenite grains grew mainly through grain boundary migration and large grain annexing the neighboring small grains.^[41] When the holding time increased from 30 to 60 seconds, the grain boundary 1 and grain boundary 2 migrated from the locations described in red dotted lines to the new locations described in yellow dotted lines by following the blue arrow paths. After migrating, the grain boundaries changed from bending to flattening, as shown in Figure 1(b). Moreover, the grain size in Figure 1(b) also was significantly larger than that in Figure 1(a). As mentioned above, the grains (grain 2, 3, 5) were annexed by grain 1 to become a larger grain (grain 7). Special to note was the grain 4 that was divided up by two grains. The top half and bottom half of grain 4 were annexed by grain 6 and grain 7, respectively.

Figure 2 showed the relationship between austenite grain sizes with the isothermal holding time and cooling time. With the holding time increased at 1200 °C, the average grain size grew unceasingly. When the holding time was prolonged from 0 to 60 seconds, the average grain size increased from 52.62 to 64.53 μm correspondingly. Moreover, the austenite grain also increased slightly in the cooling process. But as the different cooling rate, the increment of austenite grain size was correspondingly different. When the temperature cooled from 1200 °C to 1000 °C, the average grain size of sample with 0.5 °C/s cooling rate had the largest increment, which increased from 64.53 to 68.03 μm, increasing by 3.50 μm. In comparison, the average grain size increment of sample with a cooling rate of 10.0 °C/s was only 1.73 μm, which increment was only half of the former.

B. In Situ Observation of γ/α Transformation at Different Cooling Rate

After isothermal holding at 1200 °C, the austenite grain first grew slightly, and then began to decompose at the intermediate temperature. Figure 3 presented the typical HT-CLSM images of lath-shaped ferrite nucleation and growth at different locations in Ti-Zr

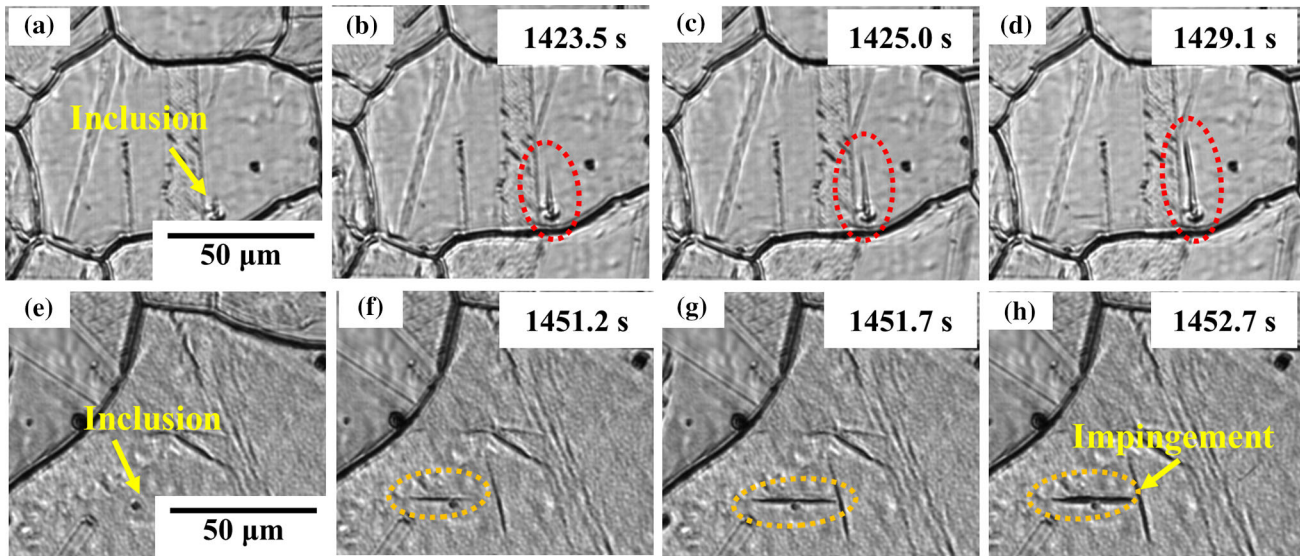


Fig. 6—Typical HT-CLSM images of AF growth of sample at 0.5 °C/s cooling rate. (a) through (d) AF was normal growth and (e) through (h) AF growth was hindered by another ferrite grain.

deoxidation steel. As Figure 3(a) showed, for the sample with 0.5 °C/s cooling rate, the ferrite lath preferentially nucleated on the grain boundary at 691.5 °C, as indicated by red dotted circle, which named as ferrite side plate (FSP) because the ferrite grew into the austenite matrix in the next time.^[42] In addition to nucleating on grain boundaries, ferrite lath also nucleated on the intragranular special inclusions. Figure 3(b) showed the ferrite lath first nucleated on the intragranular inclusion at 652.7 °C, as indicated by yellow dotted circle, which named as intragranular AF. With the temperature decreasing, the FSP and AF gradually grew up until the end of growth at 543.0 °C, as shown in Figure 3(d). The final microstructure was composed of AF and FSP, in which the proportion of AF was slightly higher than that of FSP.

With the cooling rate increasing, the ferrite lath starting transformation temperatures decreased. Similar to the sample with 0.5 °C/s cooling rate, the ferrite lath of the sample with 1.0 °C/s cooling rate also first nucleated on the grain boundary at 666.8 °C, and then the AF first nucleated on the intragranular inclusion at 644.2 °C, as shown in Figures 3(e) and (f). But compared with the former sample, the nucleated temperature was obviously lower. After the transformation finished at 530.3 °C, the final microstructure contained a large number of AF, which content was obviously higher than that of the former. Figures 3(i) through (l) showed the phase transformation of sample with 5.0 °C/s cooling rate. As noted previously, the temperature of ferrite lath first nucleated on grain boundary and intragranular inclusion were continued lower, which were at 615.9 °C and 610.8 °C, respectively. When the phase transformation was end at 500.1 °C, the final microstructure contained part bainitic ferrite (BF) that nucleated entirely in the austenite grain and appeared as parallel growth of multi-strip ferrite,^[42] replaced partial FSP and AF.

Moreover, for the sample with higher cooling rate, not only the temperature of ferrite lath first nucleated continued to lower, but also the location of ferrite lath first nucleated changed, as shown in Figure 3(m) through (p). For the sample with 10.0 °C/s cooling rate, the ferrite lath first nucleated temperature was decreased to 564.5 °C, and the ferrite lath nucleated simultaneously on the grain boundary and the intragranular inclusion at this temperature. After the phase transformation finished at 325.1 °C, the microstructure not only contained BF, FSP, and AF, as mentioned above, but also contained a few martensite (M).

The schematic continuous cooling transformation (CCT) diagram was constituted by choosing the start nucleating temperature of FSP and AF, as shown in Figure 4. The start nucleating temperature of FSP and AF decreased with increasing cooling rate.^[38,39] As we all known, the ferrite nucleation was from the decomposition of undercooled austenite. When the cooling rate was smaller, the undercooling was lower, which resulted the instability of undercooled austenite and the transition prone occur. But for the sample with higher cooling rate, the incubation period of phase transformation increased, the stability of undercooled austenite improved, which resulted the phase transition delayed and the temperature of phase transition decreased.

Furthermore, Figure 4 also revealed the difference of start nucleated temperature between FSP and AF was reduced with the cooling rate increasing. As mentioned above, undercooling was one of necessary conditions for phase transition nucleation. But for FSP and AF, the nucleation position also had some influences on the nucleation energy barrier.^[43,44] When the cooling rate was lower, the temperature decreased slowly. At this time, the contribution of undercooling to nucleation driving force was almost the same for FSP and AF, so the nucleation position played an important role. Reference 17 introduced the energy barriers of ferrite

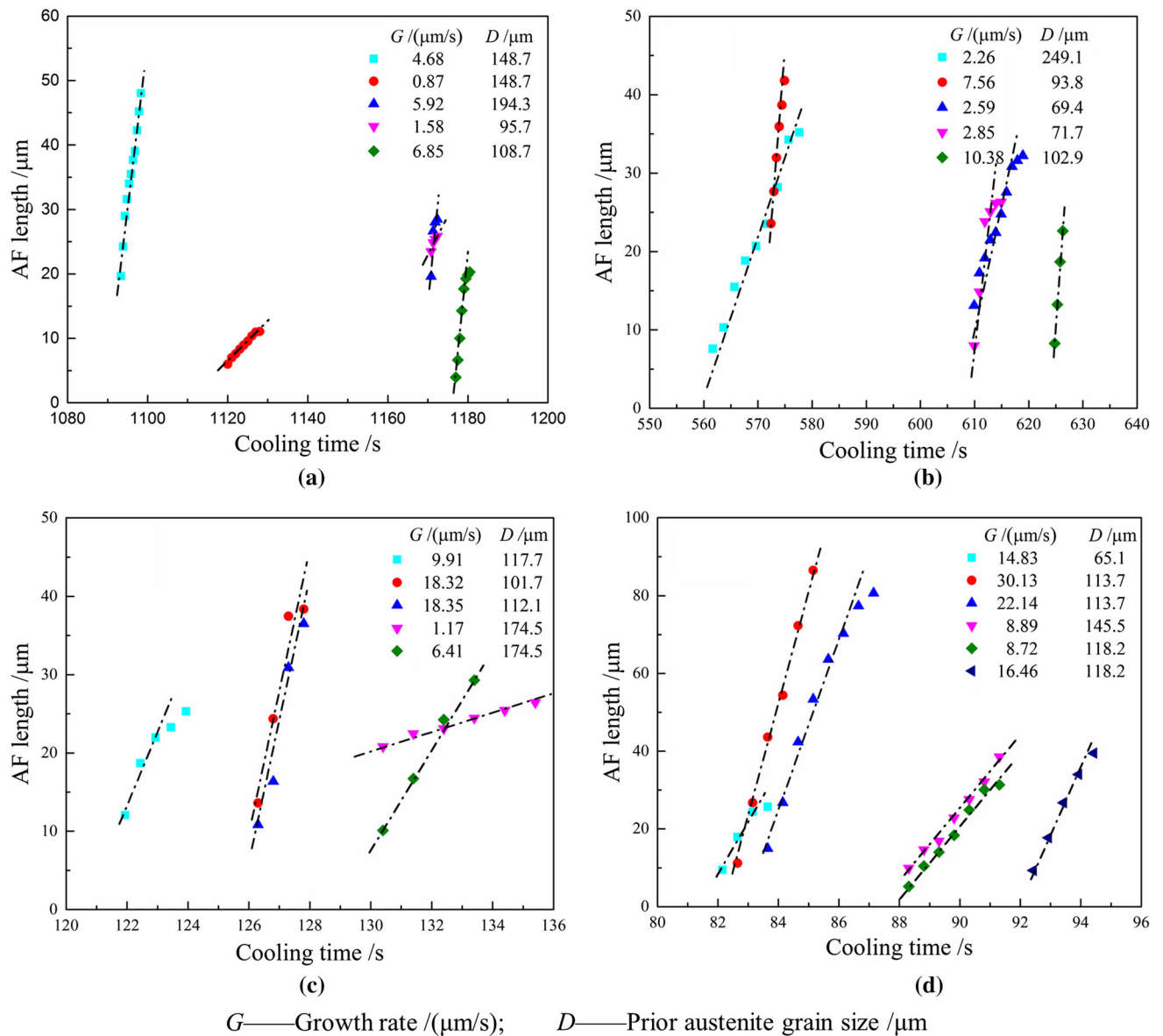


Fig. 7—Relationship between AF length and cooling time at different cooling rates (a) 0.5 °C/s, (b) 1.0 °C/s, (c) 5.0 °C/s, and (d) 10.0 °C/s.

nucleating on austenite grain boundary and inclusions. The energy barrier of ferrite nucleating on austenite grain boundary was constant, and because of the lower interfacial energy between austenite and ferrite,^[45] its nucleation energy barrier was lower.^[46] But for the energy barrier of ferrite nucleating on inclusions, it depended not only on the composition and type of inclusions, but also on the size of inclusions. For a specific inclusion, there existed a critical size that met the lowest energy barrier for ferrite nucleation. When the cooling rate was low, the driving force of ferrite nucleation was small, and the critical size of inclusion was relatively large. Therefore, if there was no large size inclusion that met the critical size in the austenite grain, the ferrite preferentially nucleated on the austenite grain boundary. However, for sample with larger cooling rate, the temperature drop was large and undercooling was

higher. At this moment, the nucleation driving force contributed by the undercooling became the main factor for ferrite nucleation, while the potential barrier at different nucleation locations could be neglected compared with the nucleation driving force. Therefore, FSP and AF could nucleate simultaneously at 564.5 °C, as shown in Figure 3(m).

The driving force for ferrite nucleation regarded as the Gibbs free energy difference between the γ phase and α phase was calculated by the software ThermoCalc-2017b and TCFE9.0 database at different temperature based on the experimental steel composition. Combining the start nucleation temperatures of FSP and AF at different cooling rate in Figure 4, the FSP and AF nucleation driving forces of each sample were obtained. Then the relationship between driving force and cooling rate was plotted, as Figure 5 illustrated.

With the cooling rate increasing, the driving force for ferrite nucleation increased. For the rapid cooling rate, a large driving force was necessary to induce FSP and AF nucleation.^[38] With regard to the sample with 10.0 °C/s cooling rate, the driving force of FSP and AF nucleation were 979.87 J/mol. But for the sample with 0.5 °C/s cooling rate, the nucleation driving force of FSP and AF were 323.82 and 497.88 J/mol, respectively, which were only about one third and a half comparing the former.

C. Growth Kinetics of AF at Different Cooling Rate

In addition to the influence of the cooling rate on the thermodynamics of AF nucleation, the cooling rate also had an effect on the AF growth kinetics.^[39] Figure 6 showed the typical HT-CLSM images of AF growth of sample with 0.5 °C/s cooling rate. After AF nucleating on the intragranular inclusion, AF length increased along optimal orientation with the increase of cooling

time. In general, the factors affecting AF growth were mainly undercooling^[47] and local element concentration differences.^[48] When the undercooling was certain and the local element concentration difference reached equilibrium, AF growth stopped and the length would no longer change, as shown in Figures 6(a) through (d). However, during the AF growth process, it often impinged with original austenite grain boundary or other AF grains to limit its growth, just as the collision of austenite grain growth.^[41] Figures 6(e) through (h) showed the process that AF growth limited by another AF grain, which made ferrite interlock each other and resulted the length of AF was little. Moreover, in the direction of width and thickness, the AF also grew, but the change of AF growth could not be observed under 2D microscopy.^[47,49] So only the growth rate in length direction would be described in the following discussion.

In order to obtain the AF growth rate, some AF laths were randomly selected from the HT-CLSM images of experimental field to observe growth and measured the AF length by IPP 6.0. Figure 7 showed the measurement results of relationship between the AFs length and cooling time of samples at different cooling rates. Due to other grain boundaries or grains hindrance during AF growth, the growth rate of each AF was significantly different. Furthermore, with the cooling rate increased, the AF growth rate difference between maximum and minimum also increased. When the sample cooling rate increased from 0.5 to 1.0, 5.0, and 10.0 °C/s, the difference of AF growth rate correspondingly increased from 5.98 to 8.12, 17.18, and 21.41 μm/s, respectively.

Growth rate was one of important parameters for studying the AF growth kinetics, and choosing which value to represent the actual growth rate was critical to the accuracy of the study results. Mu *et al.*^[34] compared several studies on AF growth rate, and considered the maximum value of AF growth rate could represent the actual growth rate. Therefore, the actual growth rates for four different cooling rate samples were 6.85, 10.38, 18.35 and 30.13 μm/s, respectively. Figure 8 showed the

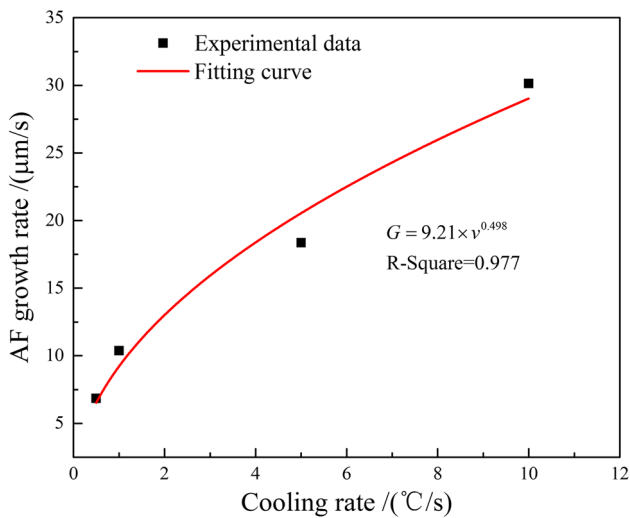


Fig. 8—Curve of AF actual growth rate varying with cooling rate.

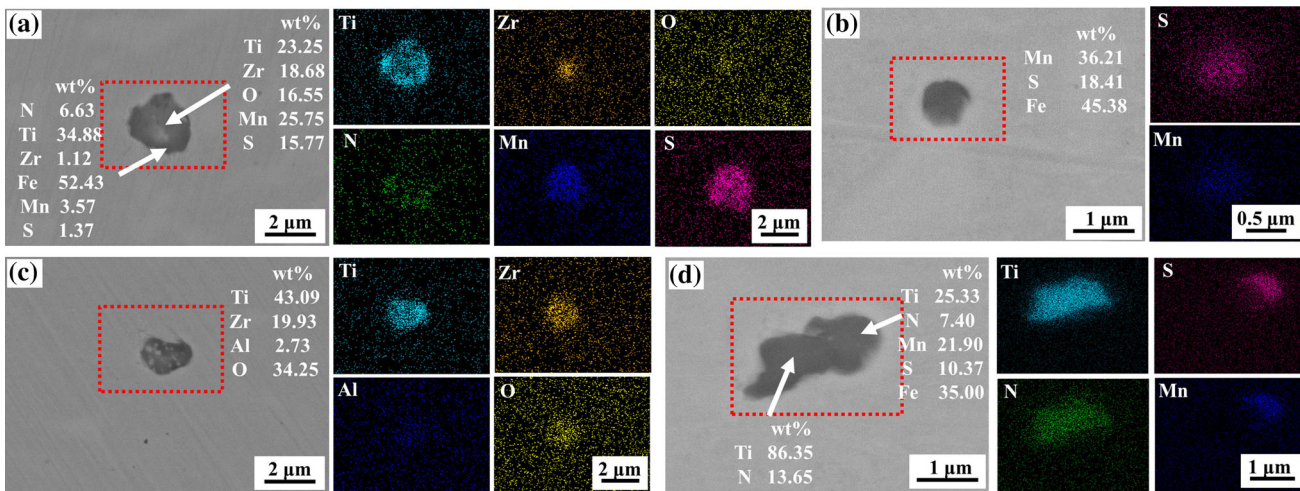


Fig. 9—SEM and EDS analyses of the typical inclusions. (a) Ti-Zr-Mn-S-O + TiN inclusion, (b) MnS inclusion, (c) Ti-Zr-Al-O inclusion, and (d) TiN + MnS inclusion.

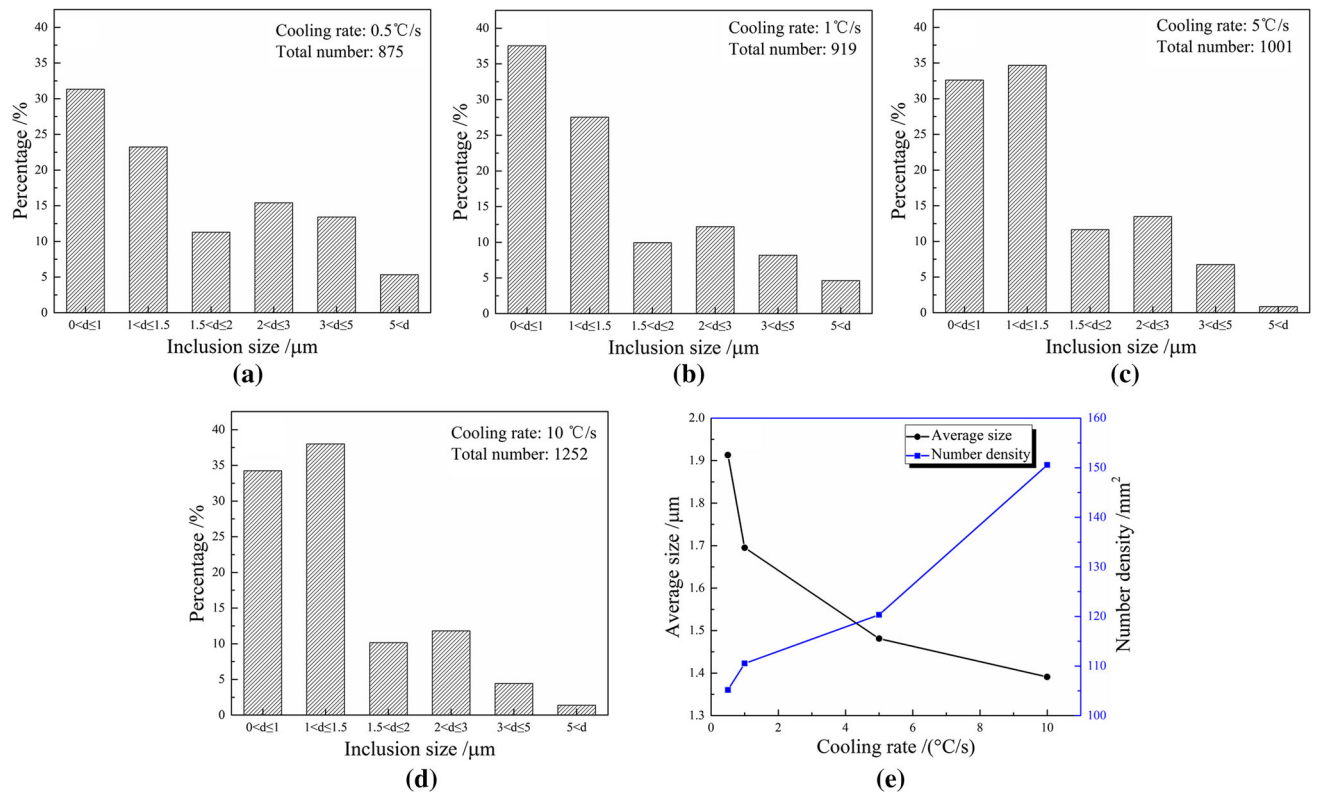


Fig. 10—Characteristics of the inclusion at different cooling rate. (a) through (d) Size distribution of inclusions and (e) average size and number density of inclusions.

relationship between AF actual growth rate and cooling rate. The actual growth rate raised with the cooling rate increased. The rule was consistent with the results of previous studies.^[39,50] As we discussed in Section III–B, when the cooling rate of sample was larger, the phase transition temperature was lower, the undercooling and driving force for AF growth were larger than the sample with lower cooling rate. Therefore, the AF actual growth rate of sample with higher cooling rate was larger than that of sample with lower cooling rate.

In order to quantify the relationship between the actual growth rate and the cooling rate, the experimental data were fitted by red curve as shown in Figure 8, and the fitting equation was shown in Eq. [1], which could predict the actual growth rate of AF at unknown experimental cooling rates.

$$G_A = 9.21 \times v^{0.498} \quad [1]$$

where G_A was the AF actual growth rate, $\mu\text{m/s}$; v was the cooling rate, $^\circ\text{C/s}$.

D. Effect of Cooling Rate on Inclusion and Microstructure

Figure 9 showed the morphology and energy spectrum analysis of the typical inclusions detected in the four samples. They were distinguished as Ti-Zr-Mn-O-S + TiN inclusion, MnS inclusion, Ti-Zr-Al-O inclusion, and TiN + MnS inclusion based on the EDS analysis. From the analysis results, the types of

typical inclusions of the four samples at different cooling rate had no difference. However, the cooling rate had a significant effect on the size distribution of inclusions.^[51] For the analysis of inclusion characteristics, 36 fields of view were randomly selected at $\times 500$ magnification by SEM, and then IPP 6.0 was used for statistical analysis. The total observation area was 8.318 mm^2 . Figure 10 showed the inclusions size distribution, average size and number density in samples with different cooling rates. As can be seen from Figures 10(a) through (d), with the increase of cooling rate, the inclusion size decreased obviously, and the proportion of large size inclusions (size $> 3.0 \mu\text{m}$) reduced gradually. When the cooling rate was increased from 0.5 to 1.0, 5.0, 10.0 $^\circ\text{C/s}$, the number of inclusions per unit area was increased, but the average size of the inclusions was decreased from 1.91 to 1.69, 1.48, and 1.39 μm , respectively, as shown in Figure 10(e). As we all know, the inclusions, as MnS and TiN, which precipitated during solidification were prone to short-range diffusion and solid solution during holding at high temperature. When the sample was cooled, the elements after diffusion and solid solution would re-aggregate to form new inclusions, and the growth of new inclusions could be considered as the Ostwald ripening process. As we explained in Section III–B, for the sample with a rapid cooling rate, the temperature of the new inclusion growth process was lower and the time was shorter. So the coarsening of new inclusion could not be obtained, which resulted the number of new small inclusions remained and not

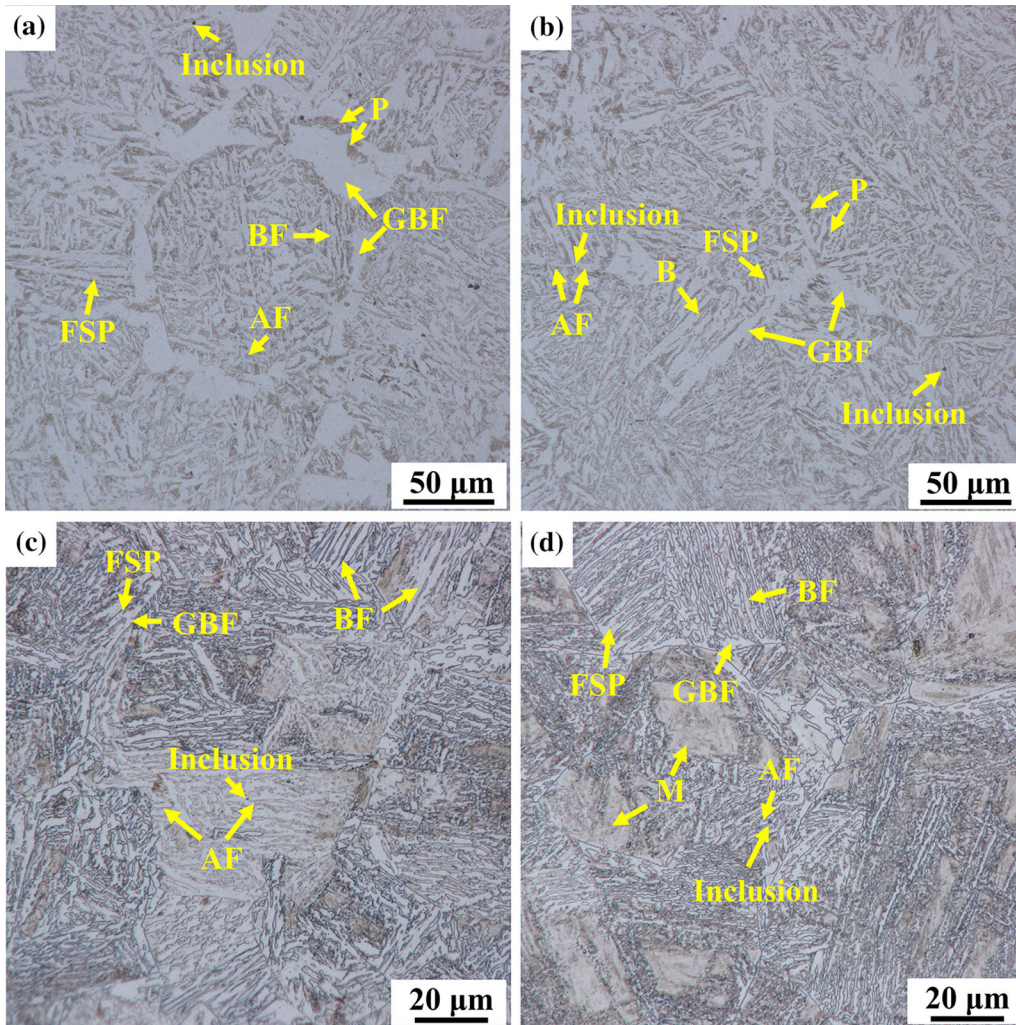


Fig. 11—Typical microstructure of samples at different cooling rate (a) 0.5 °C/s, (b) 1.0 °C/s, (c) 5.0 °C/s, and (d) 10.0 °C/s.

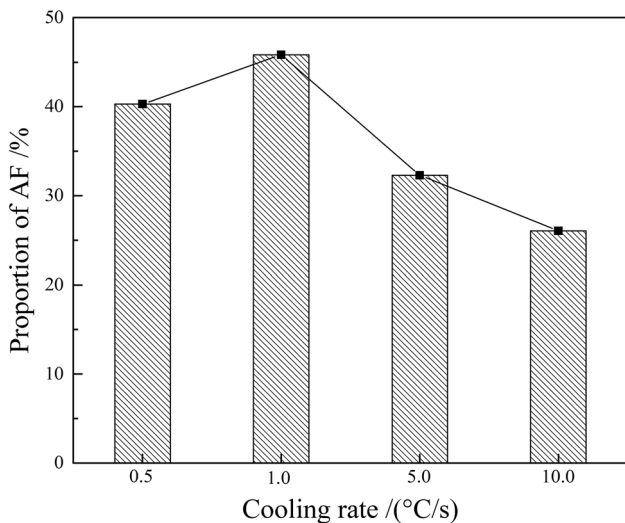


Fig. 12—Proportion of AF at different cooling rate.

dissolved by Ostwald ripening process were larger, and the average size of inclusions was smaller accordingly.

The microstructure of samples at different cooling rates was obtained, as shown in Figure 11. Combining the methods of metallographic structure and the micro-hardness of the microstructure, the microstructure types were identified. Reference 42 had given the differences of AF, FSP, BF and grain boundary ferrite (GBF) in metallographic structure, and for M in the sample of 10.0 °C/s cooling rate, it was distinguished by micro-hardness. The Vickers hardness of M was about 364.3 to 401.8, while that of other ferrite structures were about 262.1 to 293.7 that was much lower than M. When the cooling rate was 0.5 °C/s, the microstructure was mainly AF, FSP, BF, GBF and pearlite (P). When the cooling rate reached 1.0 °C/s, there was no significant change in the type of microstructure, but the AF ratio increased, while the content of GBF and FSP

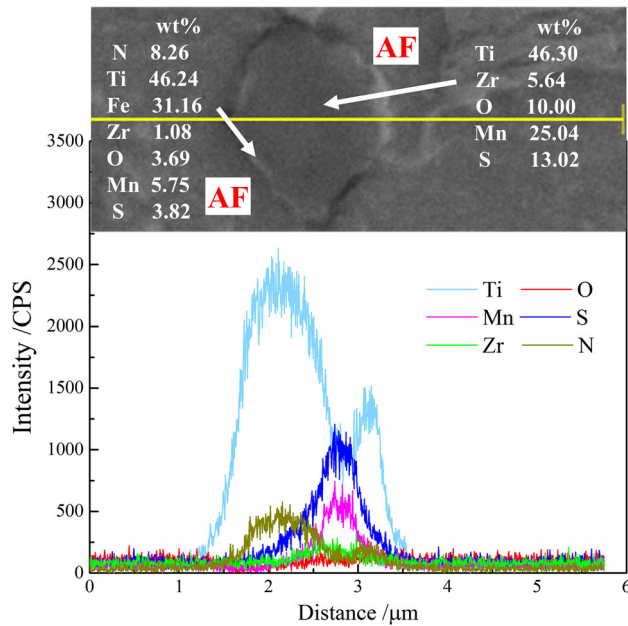


Fig. 13—Line scanning analysis of different elements along the inclusion inducing AF nucleation.

reduced. With the cooling rate increasing to 5.0 °C/s, the P disappeared and the microstructure types were mainly GBF, FSP, BF, and AF. The content of AF reduced compared to the previous two samples. As the cooling rate increasing to 10.0 °C/s, the proportion of M increased significantly, while the ratio of AF and GBF decreased markedly.

Figure 12 showed the AF ratio of four samples at different cooling rates. With the increasing of cooling rate, the proportion of AF increased first and then decreased. When the cooling rate was 1.0 °C/s, the AF ratio reached the maximum of 45.83 pct, and when the cooling rate raised to 10.0 °C/s, the AF ratio was the minimum of 26.04 pct.

It was generally known that AFs were mainly generated by heterogeneous nucleation and sympathetic nucleation^[52] In this study, the TiN + MnS inclusion and Ti-Zr-Mn-O-S + TiN inclusion were the main inclusions to induce AF nucleation. And the mechanism of TiN + MnS inclusion inducing AF nucleation was reached consensus in many literatures that were the crystal coherency of TiN with ferrite^[53,54] and the MDZ formed near inclusion.^[54] However, for the Ti-Zr-Mn-O-S + TiN inclusion, the reason of inclusion inducing AF nucleation was not clear. In previous studies,^[3,14,40] it was believed that the reason of Ti-Zr oxides induced AF nucleation was the MDZ formed near inclusion. Figure 13 showed the Ti-Zr-Mn-O-S + TiN inclusion inducing AF nucleation and the line scanning analysis of different elements along the inclusion. From the analysis results, the homogeneous Ti-Zr-Mn-O-S core was formed by the element Mn, Ti, Zr, S, and O in the center of the inclusion. In

addition, it was found that TiN was formed in the outer layer of inclusion after cooling. The lattice misfit between TiN and ferrite was small, about 4.6,^[15] which could reduce the ferrite nucleation barrier and promote the ferrite preferential nucleation on it. Therefore, we deemed the low lattice misfit between ferrite and TiN that precipitated on the surface of the Ti-Zr-Mn-O-S inclusion was one of the reasons of AF nucleation induced by the Ti-Zr-Mn-O-S + TiN inclusion. Although the higher cooling rate could produce higher thermal strain energy in the vicinity of inclusion,^[27] which was conducive to the promotion of ferrite nucleation, the strain energy produced was much smaller than the nucleation driving force.^[23] So we did not consider it as the main reason for the AF nucleation on the Ti-Zr-Mn-O-S + TiN inclusion.

These research topics on the relationship between inclusion characteristics and microstructure and the mechanism of AF nucleation will be further investigated in depth in the authors' future work.

IV. CONCLUSIONS

The effect of cooling rate on the AF nucleation, growth and the inclusion characteristics in Ti-Zr deoxidized steel were investigated by utilizing HT-LSCM. The results obtained were as follows:

- (1) With the increase of cooling rate, the ferrite nucleation temperature decreased, the driving force of ferrite nucleation rose, and the difference of nucleation temperature between AF and FSP reduced. When the cooling rate increased to 10.0 °C/s, AF and FSP simultaneously nucleated.
- (2) For samples with the increase of cooling rates, the actual growth rate of AF increased, but the AF ratio in microstructure increased first and then decreased. When the cooling rate was 1.0 °C/s, the AF ratio reached the maximum 45.83 pct.
- (3) Different cooling rates had no obvious effect on inclusion types, but had a great influence on the inclusions size distribution. With the increase of cooling rate, the number of large size inclusions in the samples decreased, and the average diameter of inclusions reduced continuously.
- (4) The low lattice misfit between ferrite and TiN that precipitated on the surface of the Ti-Zr-Mn-O-S inclusion was the main reason for Ti-Zr-Mn-O-S + TiN inclusion inducing AF nucleation.

ACKNOWLEDGEMENTS

The authors are grateful for the support from the National Natural Science Foundation of China (No. 51874081, 51574063) and Fundamental Research Funds for the Central Universities (N150204012).

REFERENCES

1. S.S. Babu and H.K.D.H. Bhadeshia: *Mater. T. JIM*, 1991, vol. 32, pp. 679–88.
2. S. Ohkita and Y. Horii: *ISIJ Int.*, 1995, vol. 35, pp. 1170–82.
3. B.W. Zhou, G.Q. Li, X.L. Wan, Y. Li, and K.M. Wu: *Met. Mater. Int.*, 2016, vol. 22, pp. 267–75.
4. Y. Shao, C.X. Liu, Z.S. Yan, H.J. Li, and Y.C. Liu: *J. Mater. Sci. Technol.*, 2018, vol. 34, pp. 737–44.
5. W.M. Mu, P.G. Jönsson, and K. Nakajima: *High Temp. Mater. Process.*, 2017, vol. 36, pp. 309–25.
6. D.S. Sarma, A.V. Karasev, and P.G. Jönsson: *ISIJ Int.*, 2009, vol. 49, pp. 1063–74.
7. X.F. Zhang, P. Han, H. Terasaki, M. Sato, and Y. Komizo: *J. Mater. Sci. Technol.*, 2012, vol. 28, pp. 241–48.
8. D. Zhang, Y. Shintaku, S. Suzuki, and Y. Komizo: *J. Mater. Sci.*, 2012, vol. 47, pp. 5524–28.
9. M.M. Song, B. Song, S.H. Zhang, Z.B. Yang, Z.L. Xue, S.Q. Song, R.S. Xu, and Z.B. Tong: *J. Iron. Steel Res. Int.*, 2018, vol. 25, pp. 1033–42.
10. Z.Z. Liu, Y. Kobayashi, F. Yin, M. Kuwabara, and K. Nagai: *ISIJ Int.*, 2007, vol. 47, pp. 1781–88.
11. Q. Huang, X.H. Wang, and M. Jiang: *Z. Y. HUSteel Res. Int.*, 2016, vol. 87, pp. 445–55.
12. M.M. Song, B. Song, C.L. Hu, W.B. Xin, and G.Y. Song: *ISIJ Int.*, 2015, vol. 55, pp. 1468–73.
13. M. Fattahi, N. Nabhani, M. Hosseini, N. Arabian, and E. Rahimi: *Micron*, 2013, vol. 45, pp. 107–14.
14. J. Pu, S.F. Yu, and Y.Y. Li: *J. Alloys Compd.*, 2017, vol. 692, pp. 351–58.
15. J.M. Gregg and H.K.D.H. Bhadeshia: *Acta Mater.*, 1997, vol. 45, pp. 739–48.
16. Y. Morikage, K. Oi, F. Kawabata, and K. Amano: *Tetsu-to-Hagané*, 1998, vol. 84, pp. 510–15.
17. W.Z. Mu, P.G. Jönsson, and K. Nakajima: *J. Mater. Sci.*, 2016, vol. 51, pp. 2168–80.
18. J.H. Shim, Y.W. Cho, S.H. Chung, J.D. Shim, and D.N. Lee: *Acta Mater.*, 1999, vol. 47, pp. 2751–60.
19. L. Cheng, C. Xu, L.L. Lu, L. Yu, and K.M. Wu: *J. Alloys Compd.*, 2018, vol. 742, pp. 112–22.
20. W.Z. Mu, P.G. Jönsson, and K. Nakajima: *ISIJ Int.*, 2014, vol. 54, pp. 2907–16.
21. I. Madariaga, J.L. Romero, and I. Gutiérrez: *Metall. Mater. Trans. A*, 1998, vol. 29A, pp. 1003–15.
22. X.B. Li, Y. Min, C.J. Liu, and M.F. Jiang: *Steel Res. Int.*, 2016, vol. 87, pp. 622–32.
23. C.K. Lin, Y.C. Pan, Y.H.F. Su, G.R. Lin, W.S. Hwang, and J.C. Kuo: *Mater. Charact.*, 2018, vol. 141, pp. 318–27.
24. Z. Zhang and R.A. Farrar: *Mater. Sci. Technol.*, 1996, vol. 12, pp. 237–60.
25. W.Z. Mu, H.H. Mao, P.G. Jönsson, and K. Nakajima: *Steel Res. Int.*, 2016, vol. 87, pp. 311–19.
26. B. Wen, B. Song, N. Pan, Q.Y. Hu, and J.H. Mao: *Ironmak. Steelmak.*, 2011, vol. 38, pp. 577–83.
27. S.H. Zhang, N. Hattori, M. Enomoto, and T. Tarui: *ISIJ Int.*, 1996, vol. 36, pp. 1301–09.
28. B.L. Bramfitt: *Metall. Mater. Trans. B*, 1970, vol. 1A, pp. 1987–95.
29. M. Militzer, R. Pandi, and E.B. Hawbolt: *Metall. Mater. Trans. A*, 1996, vol. 27, pp. 1547–56.
30. C.J. Shang, L.J. Hu, S.W. Yang, X.M. Wang, Y.T. Zhao, and X.L. He: *Acta Metall. Sin.*, 2005, vol. 41, pp. 471–76.
31. G. Thewlis, J.A. Whiteman, and D.J. Senogles: *Mater. Sci. Technol.*, 1997, vol. 13, pp. 257–74.
32. Y.C. Liu, D.J. Wang, F. Sommer, and E.J. Mittemeijer: *Acta Mater.*, 2008, vol. 56, pp. 3833–42.
33. Y.J. Kang, S.H. Jeong, J.H. Kang, and C.H. Lee: *Metall. Mater. Trans. A*, 2016, vol. 47A, pp. 2842–54.
34. W.Z. Mu, P. Hedström, H. Shibata, P.G. Jönsson, and K. Nakajima: *JOM*, 2018, vol. 70, pp. 2283–95.
35. W.Z. Mu, N. Dogan, and K.S. Coley: *JOM*, 2018, vol. 70, pp. 1199–1209.
36. T. Hanamura, H. Shibata, Y. Waseda, H. Nakajima, S. Torizuka, T. Takanashi, and K. Nagai: *ISIJ Int.*, 1999, vol. 39, pp. 1188–93.
37. D. Zhang, H. Terasaki, and Y. Komizo: *Acta Mater.*, 2010, vol. 58, pp. 1369–78.
38. W.Z. Mu, H. Shibata, P. Hedström, P.G. Jönsson, and K. Nakajima: *Steel Res. Int.*, 2016, vol. 87, pp. 10–14.
39. X.D. Zou, J.C. Sun, H. Matsuura, and C. Wang: *Metall. Mater. Trans. B*, 2018, vol. 49A, pp. 2168–73.
40. M. Wakoh, T. Sawai, and S. Mizoguchi: *Tetsu-to-Hagané*, 1996, vol. 82, pp. 593–98.
41. X.L. Wan, K.M. Wu, G. Huang, R. Wei, and L. Cheng: *Int. J. Min. Met. Mater.*, 2014, vol. 21, pp. 878–85.
42. D. Zhang, Y. Shintaku, S. Suzuki, and Y. Komizo: *Metall. Mater. Trans. A*, 2012, vol. 43A, pp. 447–58.
43. S.I. de Bott and P.R. Rios: *Scripta Mater.*, 1998, vol. 38, pp. 1269–74.
44. J.S. Liu and J. Yanagimoto: *ISIJ Int.*, 2007, vol. 47, pp. 1188–94.
45. J.S. Byun, J.H. Shim, Y.W. Cho, and D.N. Lee: *Acta Mater.*, 2003, vol. 51, pp. 1593–06.
46. H.K.D.H. Bhadeshia and J.W. Christian: *Metall. Mater. Trans. A*, 1990, vol. 21A, pp. 767–97.
47. L. Cheng and K.M. Wu: *Acta Mater.*, 2009, vol. 57, pp. 3754–62.
48. M.M. Hosseinioun and G. Moeini: *Mater. Test.*, 2016, vol. 58, pp. 848–59.
49. K.M. Wu, Y. Inagawa, and M. Enomoto: *Mater. Charact.*, 2004, vol. 52, pp. 121–27.
50. C.K. Lin, Y.C. Pan, W.S. Hwang, Y.C. Fang, Y.H. Su, G.R. Lin, and Y.F. Wu: *Ironmak. Steelmak.*, 2019, vol. 46, pp. 176–83.
51. N. Kikuchi, S. Nabeshima, T. Yamashita, Y. Kishimoto, S. Sridhar, and T. Nagasaka: *ISIJ Int.*, 2011, vol. 51, pp. 2019–28.
52. S.S. Babu: *Curr. Opin. Solid. State Mater. Sci.*, 2004, vol. 8, pp. 267–78.
53. H.H. Jin, J.H. Shim, Y.W. Cho, and H.C. Lee: *ISIJ Int.*, 2003, vol. 43, pp. 1111–13.
54. Y. Tomita, N. Saito, T. Tsuzuki, Y. Tokunaga, and K. Okamoto: *ISIJ Int.*, 1994, vol. 34, pp. 829–35.

Publisher's Note Springer Nature remains neutral with regard to jurisdictional claims in published maps and institutional affiliations.